HHS Public Access

Author manuscript

Curr Biol. Author manuscript; available in PMC 2022 July 26.

Published in final edited form as:

Curr Biol. 2021 July 26; 31(14): 3115–3124.e5. doi:10.1016/j.cub.2021.05.008.

One-to-one innervation of vocal muscles allows precise control of birdsong

Iris Adam[1], **Alyssa Maxwell**[1], **Helen Rößler**[1], **Emil B. Hansen**[1], **Michiel Vellema**[1], **Jonathan Brewer**[2], **Coen P.H. Elemans**[1,*]

[1]Department of Biology, University of Southern Denmark, Campusvej 55, 5230 Odense, Denmark

[2]PhyLife, University of Southern Denmark, Campusvej 55, 5230 Odense, Denmark

Summary

The motor control resolution of any animal behavior is limited to the minimal force step available when activating muscles, which is set by the number and size distribution of motor units (MUs) and muscle specific force. Birdsong is an excellent model system for understanding acquisition and maintenance of complex fine motor skills, but we know surprisingly little how the motor pool controlling the syrinx is organized and how MU recruitment drives changes in vocal output. Here we developed an experimental paradigm to measure MU size distribution using spatiotemporal imaging of intracellular calcium concentration in cross-sections of living intact syrinx muscles. We combined these measurements with muscle stress and an *in vitro* syrinx preparation to determine the control resolution of fundamental frequency (f_0), a key vocal parameter, in zebra finches. We show that syringeal muscles have extremely small MUs, with 40 – 50 % innervating ≤ 3, and 13 – 17% innervating a single muscle fiber. Combined with the lowest specific stress (5 mN/mm^2) known to skeletal vertebrate muscle, small force steps by the major f_0 controlling muscle provide control of 50 mHz to 7.3 Hz steps per MU. We show that the song system has the highest motor control resolution possible in the vertebrate nervous system and suggest this evolved due to strong selection on fine gradation of vocal output. Furthermore, we propose that high-resolution motor control was a key feature contributing to the radiation of songbirds that allowed diversification of song and speciation by vocal space expansion.

eTOC Blurb

Adam et al. show that the zebra finch vocal motor pool has extremely small motor units, with 13–17% of motor neurons innervating single syringeal muscle fibers. Together with very low muscle stress, this high-resolution motor control allows for fine control of vocal output, including sub-Hz pitch control, leading to vocal space expansion.

*Correspondence and Lead Contact: coen@biology.sdu.dk.

Author Contributions. Conceptualization, IA, CPHE; Methodology, IA, AM, JB, CPHE; Software, IA, CPHE; Formal Analysis, IA, AM, CPHE; Investigation, IA, AM, HR, EBH, MV, CPHE; Writing – Original Draft, CPHE; Writing – Review & Editing, IA, AM, CPHE; Funding Acquisition, IA, CPHE; Resources, IA, JB, CPHE; Supervision, CPHE.

Declaration of Interests. The authors declare no competing interests.

Keywords

birdsong; motor control; motor unit; songbird; sound production; vocal communication; voice

Introduction

Vocal communication is of paramount importance for reproduction and survival of songbirds and even drives speciation. This is clearly exemplified by sympatric species that are morphologically indistinguishable, but nevertheless fully separated solely by song [1, 2]. The potential to acoustically separate depends on the number of distinct sounds - or vocal space - that can be produced and perceived. The vocal space is set both by the range available to vary an acoustic feature, and in what steps, or resolution, the feature can be controlled within this range. Thus, both resolution and range expand the vocal space and may form a rich substrate for species diversification [3, 4]. While the range of an acoustic feature, for example f_0, is typically limited by intrinsic constraints of the vocal organ [5–7], the ability to generate distinct f_0 changes within these constraints is set by the resolution of the neural control. In contrast to the well-described neural circuitry underlying song learning [8], we know little about the organization of the motor pool controlling the songbird syrinx [9]. Furthermore, even though birdsong is often called a fine-motor skill [10, 11] and perturbed auditory feedback can drive small f_0 changes [12, 13], the control resolution of acoustic features remains unknown.

The minimal force step available when activating muscles sets the minimal motor control resolution of any behavior and is set by the number and size distribution of motor units (MUs) and muscle fiber specific force generation [14]. A MU is the basic functional unit of skeletal muscle and consists of a motor neuron and the number of muscle fibers it innervates, aka the innervation number (*IN*). Variation in *IN,* muscle specific force and spike rate are the most significant factors to contribute to differences in MU force in skeletal muscles [14]. Currently, we do not know the minimal force step available in vocal motor control and how MU recruitment causes changes in vocal output in songbirds [15].

Here we combine measurements of syringeal muscle innervation numbers and MU *IN* distributions with muscle stress and an *in vitro* syrinx preparation to estimate the control resolution of f_0, a key vocal parameter, in zebra finches. Our results reveal that syringeal muscles have extremely small MUs and suggest that 13 – 17% of the motor neurons innervate a single muscle fiber. Together with the lowest specific stress (5 mN/mm^2), small force steps provide f_0 control of as small as 50 mHz to 7.3 Hz steps per MU. This one-to-one innervation provides the song system with the highest motor control resolution possible.

Results

MU distributions predict one-to-one innervation in the songbird syrinx motor pool

We quantified the mean *IN* (IN_{mean}) of syringeal muscles in male zebra finches by counting *i)* the number of muscle fibers per syrinx side and *ii)* the number of axons in the supplying ipsilateral nerve within individuals (Figure 1, Table S1, See Methods). The average number

of axons in the tracheosyringeal branch of the hypoglossal nerve (NXIIts), was 809 ± 167 (n = 13) and did not differ significantly between left and right (Table S1). The average number of muscle fibers per hemisyrinx was higher on the right side compared to the left (left: 3234 ± 232, n = 4; right: 3794 ± 334, n = 4, p = 0.04) (Figure 1E). The total number of muscle fibers was 6995 ± 789 (n = 4), corroborating earlier reported ~6730 [16], while our axon counts are lower, but within range of the 1026 ± 126 (n = 6) reported earlier [17]. To estímate the number of motor units, we assumed the fraction of sensory axons to be between 0 and 33% (See methods) [17, 18]. The IN_{mean} per hemisyrinx and individual was 4.78 ± 0.75 on average, (range: 3.85 – 5.67, n = 7) when assuming 0% sensory axons, and 7.25 ± 1.13 (range: 5.83 – 8.59, n = 7) when assuming 33% sensory axons (Figure 1F). Vertebrate muscles typically have *INs* of several hundred muscle fibers [14]. The IN_{mean} of syringeal muscles is thus extremely low, and comparable only to, but still lower than, laryngeal [19, 20] and extraocular [21] muscles.

However, critical to muscle function is not the IN_{mean} among MUs, but the *IN* distribution within a given motor pool [14, 23]. *IN* distribution sets the smallest force step possible and the motor pool proportions that innervate different muscle fiber types [14]. The frequency distribution of MU size has been approximated based on force output in skeletal muscles [24–27] and more recently measured directly in anatomical connectome reconstructions of a mouse craniofacial [28] and forepaw muscle [29]. Both methods result in MU size distributions that are consistently skewed for all muscles studied to date [24–29]: the majority of MUs are small and only few are large (Figure 2A). The MU-size distribution in all cases is best described by an exponential distribution (Figure 2A, S1; See methods).

We estimated the frequency distribution of MU size within syringeal muscles by exploiting these distributions (See methods). Using our anatomical data on the number of MUs and muscle fibers, we systematically varied (Figure 2B) the size of the smallest and largest MU to find the value where the predicted number matches the counted number of muscle fibers (Figure 2C). About 87 *%* of all muscle fibers in adult male zebra finches seem of the superfast phenotype [16, 30]. Including only superfast fibers (red lines in Figure 2B, 2C, S2, Methods) and 0 % sensory afferents, we predict that syringeal MUs range in size from 1 to 11.9 ± 2.5 (range of maximal MU size: 9 – 15, n = 7) muscle fibers. As a consequence, half of all syringeal MUs (51 ± 5 %, n = 7) innervate as few as ≤ 3 muscle fibers, and 17 ± 1 % of the MUs innervate a single muscle fiber (Figure 2D, 2E). Using the most conservative estimate of 33 % sensory axons in NXIIts, we predict that superfast syringeal MUs contain 1 to 21.1 ± 4.4 muscle fibers (range of maximal MU sizes 16 – 27, n = 7). 41 ± 3 % of all motor neurons innervate as few as ≤ 3 muscle fibers and 13 ± 1 % only one single superfast syringeal muscle fiber. Such one-to-one anatomical innervation has to our knowledge only been reported for monkey extraocular muscle [31] and one motor neuron of the mouse interscutularis muscle [28].

The songbird syrinx motor pool has the highest control resolution possible

To confirm that the syrinx motor pool indeed can control individual muscle fibers and that the exponential distribution models are applicable, we developed a novel experimental paradigm to measure MU size distribution within an intact nerve-muscle prep *in vitro* (See

methods). We electrically stimulated sections of the fanned motor nerve and detected the spatiotemporally resolved intracellular calcium concentration in all MFs of an entire muscle. We imaged the muscle cross-section using a fast translation stage mounted on a multi-photon confocal microscope (Figure 3A) and measured the change in fluorescent intensity (dFF) of an intracellular calcium indicator. In the excitation-contraction coupling pathway of a vertebrate skeletal muscle, an action potential from the motor neuron crosses the neuromuscular junction and results in calcium release from the sarcoplasmatic reticulum [32]. The intracellular calcium concentrations should thus rise simultaneously in all muscle fibers that belong to the same MU and the dFF patterns can consequently be used to identify MFs that belong to the same MU.

Achieving tissue penetration deeper than 50 μm with confocal microcopy is difficult in muscle due to the crystalline organization and protein density of muscle [33]. However, by matching the refractory index to the relatively thin dorsal syrinx muscle (MDS) we achieved full optical penetration of 80 μm and could identify all 170 ± 20 MFs (n = 4) in the intact live muscle cross-section (Figure 3C). To test the fraction of living fibers after the dissection procedure, we applied repetitive field stimulations to the entire muscle and tested for all individual MFs if the dFF signal (Figure 3D) increased significantly over baseline (at $p = 0.01$). 95 ± 2 % of MFs were alive in the preparations (n = 4).

Next, we applied repetitive (4 Hz) electrical stimulation to different sections of the fanned motor nerve with an array of electrodes while measuring dFF of all muscle fibers at 31 Hz (Figure 3E, 3F, Video S1). To have fine-control over the amount of injected energy, we increased the stimulus duration by 10 μs steps at constant current. Because MUs have different activation thresholds due to variation in axonal diameters [34], the slow increasing stimulation strength separated the onset of different MUs in time and energy step (Figure 3G). By comparing temporal patterns (Figure 3G) and threshold crossings (Figure 3H) of the time-resolved dFF patterns between all muscle fibers, we could identify all active MUs per electrode and measure their *IN.*

We found MUs consisting of single muscle fibers in all individuals (n = 4, Figure 3I). The MU sizes across all animals and electrodes ranged from 1 to 9 muscle fibers. The summed distribution followed the exponential model we employed to estimate the distribution of our anatomical data (Figure 3I, 3J) and falls within known distributions [24–29].

Taken together, our data strongly suggest that one-to-one innervation occurs in the syrinx motor pool and that the most commonly used MU size distribution model holds for syringeal muscles. The nXIIts motor pool is thus equipped with the highest control resolution possible in the vertebrate nervous system: one-to-one innervation.

Songbird syringeal muscles generate the lowest stress

The other determinant of MU force is set by the stress (P) it generates. Stress depends on muscle-specific intrinsic properties [14] combined with rate and timing of motor neuron firing [35]. Stress ranges from the peak stress during the all-or-none twitch contraction (P_{tw}) caused by a single motor neuron spike on the lower end, up to the maximum stress during tetanic contraction (P_o) caused by spike trains of the motor neuron. Because syringeal

muscles are superfast muscles that can power movement up to 200 – 250 Hz [36], they trade force for speed as a fundamental architectural trait [30, 37] and are expected to have low P_o. Indeed, pigeon syringeal muscles generate a P_o as low as 18 – 50 mN/mm^2 [38], 5 – 10 times lower as regular skeletal muscle fibers (~150 – 300 mN/mm^2) [39, 40] (Figure 4E), but the P_o of songbird syringeal muscles is unknown.

We measured stress generated by syringeal muscles on isolated fiber bundles *in vitro* for twitch (P_{tw}) and tetanic (P_o) contractions after a series of length and stimulus amplitude and frequency optimizing experiments (Figure 4A – D). We focused on the ventral syringeal muscle (VS) that predominantly controls fundamental frequency (f_o) or pitch [41–43]. Because VS fibers proved difficult to isolate, we added two other syringeal muscles, VTB and DTB, that control airflow though the syrinx [44]. P_o did not differ between syringeal muscles and measured 5.21 ± 6.04 mN/mm^2 (range = 0.64 – 15.4 mN, n = 5) for VS and 5.97 ± 4.46 mN/mm^2 (range = 0.64 – 15.4 mN, n = 17) for all muscles combined (Figure 4F). Combining P_{tw}, P_o, cross-sectional area (CSA) and the number of muscle fibers for each muscle (Table S1) provides the maximum force (tetanic stimulation) produced by the entire muscle (Figure 4G) and the minimum force (single twitch) per single muscle fiber (Figure 4H). As such, on average VS force ranged from 0.86 ± 1.00 μN (single twitch in a single fiber) up to 5.31 ± 6.16 mN (full tetanic contraction of the entire muscle). The P_o of syringeal muscles is 2 and 3 times lower than P_o of superfast muscles found in bat (9.4 ± 4.2 mN/mm^2) (See methods) and toadfish (15 – 24 mN/mm^2) [45, 46], four times lower than pigeon syrinx muscles [38], 30 times lower than zebra finch flight muscles [47], and up to 60 times lower than mammalian limb muscles [39, 40]. Thereby syrinx muscles have the lowest P_o of any vertebrate skeletal muscle to our knowledge.

Syringeal MUs provide sub-Hertz resolution control of fundamental frequency

To study the effect of MU recruitment on vocal output, we focused on the control of f_o, an important cue in vocal communication [6]. In birds, analogous to mammalian vocal fold vibrations, expiratory airflow from the bronchi induces self-sustained vibration of vocal fold-like structures, the labia, within the syrinx [48]. In zebra finches, radiated sound pulses are tightly associated with labial collision within the vibration cycle and labial vibration frequency thus directly sets f_o [42]. When VS shortens, it lengthens the labia and nonlinearly increases their stiffness perpendicular to the expiratory airflow [7]. Together, this stiffness and length increase change the labial resonance frequency, which predominantly increases the labial vibration frequency [5, 7, 49]. By these mechanisms VS force controls f_o, and indeed VS multiunit EMG activity *in vivo* positively correlates to f_o [41, 43], and VS stimulation *ex vivo* causes f_o increase [42]. However, it is unknown how the MU force distribution in VS drives changes in f_o.

To quantify the effect of VS force on f_o, we developed an *in vitro* paradigm that allowed for servo-controlled actuation of muscle insertion sites, combined with simultaneous measurement of muscle shortening and force, during sound production in the syrinx (Figure 5A, See methods). Labial vibration and sound production were induced by increased bronchial and air sac pressure, while actuating the VS insertion site up to 12 % shortening of the VS muscle length (Figure 5B) [7]. Frequency transforms linearly with VS force over the

full VS force range of 0 – 5.31 mN in three out of five preparations (Figure 5C, Table S2, See methods), and over 65 – 86 % of the full VS force range of the remaining two. The linear slopes ranged from 5 – 57 Hz/mN (mean: 26.6 ± 19.4 Hz/mN, n = 5, Table S2). Because the mechanical properties of the labia are nonlinear [7, 50], this linearization of force to f_0 transformation is surprising. We propose this linearization as a beautiful example of morphological computation, where the body locally computes Solutions to simplify motor control [51].

Combining the MU distribution, P_{tw}, and P_o with the muscle force to f_0 transform, we estimated the force and f_0 distribution available to zebra finches (Figure 5D, 5E). Recruiting one of 20 – 38 MUs containing a single muscle fiber ($IN = 1$) with a single spike leads to a mean VS force increase of a mere 0.85 μN and f_0 increase of 50 mHz (Figure 5D). Full tetanic stimulation this MU results in mean VS force increase of 4.9 μN and f_0 increase of 0.3 Hz. Recruitment of the largest, single, MU containing 15 – 26 muscle fibers by full tetanic contraction leads to a mean VS force and f_0 increase between 73 – 126 μN and 4.2 – 7.3 Hz, respectively. Taking all smallest MUs together provides a f_0 gradation within a range of 5.6 – 11 Hz, and all second smallest MUs a range of 14 – 26 Hz. Thus, the full range of force and f_0 step sizes varies between 0.85 – 126 μN and 50mHz – 7.4 Hz respectively. Both suboptimal spike rates or timing codes [35] and lateral force transmission [52, 53] result in lower force production by individual muscle fibers compared to maximal stress during isometric activation. Therefore, the minimal force and vocal features steps presented here can be considered conservative estimates and are likely even smaller during song.

Discussion

Taken together, we show that the syringeal muscle motor pool has one-to-one innervation and thereby the highest control resolution possible in the vertebrate nervous system. Combined with the lowest muscle specific stress known in any vertebrate muscle, it allows f_0 control from as small as 50 mHz to 7.3 Hz steps during sound production.

Behavioral selection on resolution drove small MUs

The fine resolution motor control of f_0 our data suggest is behaviorally relevant. Zebra finch [54] and Bengalese finch males [12] can drive f_0 changes below 1 Hz, by altered auditory feedback, which corresponds to our estimate of full activation of a single muscle fiber MU. Such small f_0 changes could thus be driven by recruitment of one additional single MU. Moreover, zebra finch females are not only capable of detecting acoustic fine structure [55] and small f_0 changes below 1 Hz [56], they importantly also base their mating decision on those [57]. From a motor control perspective, this suggests a strong selection for small force steps, which can be achieved by small MU sizes combined with low specific force. As a result of the selection on muscle speed, muscle specific force reduces significantly due to architectural constraints of skeletal muscles [30]. Thus, if the force per MU should remain constant and specific force reduced 20 times, MUs could have become 20 times larger to compensate for the force-speed trade-off. However, instead we observe extremely small MUs (13 – 17 % of all MUs are innervated one-to-one), which strongly suggests an additional selection for small MUs.

MU innervation numbers below 10 are on the extremely low end of MU sizes in vertebrates, and have so far only been reported for laryngeal [19, 20], extraocular [21, 58] and ear muscles [28]. Interestingly, all those muscles belong to the craniofacial lineage [30], suggesting that their developmental origin might predispose them or even provide unique access to low MU sizes. Thus, developmental origin may in part explain the ability to achieve fine force gradation through small MUs.

Fine-resolution motor control in songbirds allows vocal space differentiation

Songbirds have radiated explosively ~40 MYA ago [59], which has been attributed to two key events. First, the evolution of syrinx morphology that may have allowed uncoupled control of specific acoustic features, such as f_o and amplitude [4, 22], thereby vastly increasing the possibilities or feature space of syllables produced. Second, the evolution of specialized neural circuitry that allowed vocal imitation by trial-and-error learning [8] providing means to explore the vast control space. However, to precisely control their vocal organ to execute trial-to-trial variability, songbirds need fine gradation of force. The songbird syrinx morphology is highly conserved [60] and has comparable numbers of muscle fibers [16] and motor neurons [61] across a wide range of songbird species, which suggests that all songbirds have access to small MUs. We suggest that small MUs were a crucial third key innovation to allow for the fine control of song, one that was pivotal to successfully expanding the acoustic feature space of songbirds, and impetus for the adaptive radiation of today's roughly 5,000 species of songbirds.

Star Methods

Resource availability

Lead contact.—Further Information and requests for resources and reagents should be directed to and will be fulfilled by the lead contact, Coen Elemans (coen@biology.sdu.dk).

Materials availability.—This study did not generate new unique reagents.

Data and code availability.—Code and source data for figures in the paper is available upon request.

Experimental Model and Subject Details

Animal use and care.—Adult male and female zebra finches (*Taeniopygia guttata)* were kept in group aviaries at the University of Southern Denmark, Odense, Denmark on a 12 h light:dark photoperiod and given water and food *ad libitum.* All experiments were conducted in accordance with the Danish law concerning animal experiments and protocols were approved by the Danish Animal Experiments Inspectorate (Copenhagen, Denmark).

Method Details

Syrinx extraction.—Animals were euthanized by Isoflurane overdose (Baxter, Lillerød, Denmark). The syrinx was dissected out through a ventral incision along the sternum, with regular flushing with oxygenated Ringer's solution, and submerged in a bath of oxygenated Ringer's on ice upon removal [38].

Muscle fiber and motor unit counts.—To measure the innervation numbers of syrinx muscles, we counted the number of muscle fibers in the syrinx and axons in the tracheosyringeal branch of the hypoglossal nerve (NXIIts) on both sides within the same individual of 8 adult male zebra finches.

The syrinx was fixed in 4 % PFA in PBS (w/v) for 24 h while keeping the rostro-caudal axis straight. Subsequently it was kept in PBS for 24 h and then embedded in Tissue-Tek O.C.T compound (Sakura Finetek), frozen and stored at −80 °C until further processing.

All specimens were cut into 10 μm serial cross-sections using a cryotome (Leica CM1860). Immunostainings were performed according to standard protocols using primary antibodies raised against Laminin (10 μg/ml, polyclonal rabbit-anti-Laminin, Sigma-Aldrich Cat# L9393, RRID: AB_477163) and Neurofilament (5 μg/ml, monoclonal mouse-anti-Neurofilament, Millipore Cat# CBL212, RRID: AB_93408) to delineate fiber-boundaries and axons respectively. Co-labeling was visualized using donkey-anti-mouse-Alexa-Fluor-568 (Abcam Cat# ab175700) and donkey-anti-rabbit-Alexa-Fluor-488 (Abcam Cat# ab150061, RRID: AB_2571722). Slides were coverslipped with Vectashield mounting medium (Vector Laboratories Cat# H-1000, RRID: AB_2336789) and sealed with transparent nail polish.

Images were acquired with a Zyla sCMOS camera (AndorTM Technology Ltd, Northern Ireland) mounted on a Nikon Eclipse T*i* inverted microscope with automated XY-stage. To count the number of muscle fibers, we acquired images from sections with a 20x objective directly rostral of bronchial bone B2, a cross-sectional plane where all muscle fibers are present [22]. In zebra finches motor endplates are located in the central region of syrinx [62], which strongly suggests there are no serial fibers. To cover the entire syrinx cross-section, we acquired 600 – 800 images in random order and stitched them together with NIS-Elements (Nikon). Muscles were counted on 10x bicubic down-sampled images (minimal image size: 5314×4293 pixels). We counted laminin and neurofilament double positive axons in images acquired with a 100x objective from sections in the region of tracheal ring T4 - T6 (minimal image size: 2561×3996 pixels). Three independent observers (IA, AM, BJ) counted muscle cells and axons using the ImageJ Cell Counter plugin. We used the mean value of these three observers for all counts.

To estimate the number of motor units from NXIIts axon counts, we corrected for the number of afferent sensory axons. NXIIts contains 1% unmyelinated axons in histological sections of NXIIts that are assumed to be sensory afferents [17]. Because we counted laminin and neurofilament double positive axons, we assumed that our counts do not include unmyelinated axons. Based on retrograde tracing from NXIIts [18], the somata of the motor neurons innervating the syrinx are located in nXIIts, while the somata of sensory neurons are located in the jugular vagal ganglion [63, 64]. Thus, the number of motor neuron somata in nXIIts equals the amount of motor neuron axons in NXIIts. To estimate the number of motor units in NXIIts, we used the two most extreme values: i) NXIIts does not contain any sensory axons and all counted axons are motor neurons. ii) NXIIts contains 33 *%* sensory axons, which is the lowest published number of motor neurons in nXIIts (780, ref [18]), divided by our highest axonal count (1162).

MU size distribution estimates.—The frequency distribution of MU size based on MU force [24–27] or anatomical connectome reconstructions [28, 29] are consistently skewed to small units for all muscles studied to date. The MU size frequency distribution follows the exponential curve:

$$y_i = y_1 e^{[\ln(R)/n] \times i}, \quad \text{Eq 1}$$

where y_i is the innervation number of MU *i*, y_1 is the innervation number for the smallest MU (unit 1), n is the number of MUs, and R is the ratio of innervation numbers for the largest and smallest unit: $R = y_n/y_1$ [65]. We fitted Eq 1 to force-based or connectome-based MU size distributions by iteratively optimizing the model through minimizing least squares using the MATLAB routine *lsqcurvefit.*

To estimate the distribution of MUs within syringeal muscles, Eq 1 allowed us to calculate the number of muscle fibers within the muscle (N_{MF}) for a given maximum MU size as $N_{MF} = \sum_{i=1}^{n} y_i$. Thus, by knowing N_{MF} for a muscle, we can calculate the maximum MU size and MU size distribution.

The cumulative fraction of muscle fibers with MU number allows for consideration of muscle fiber type when calculating distributions [14]. About 87 % of all muscle fibers in adult male zebra finches do not react to fast myosin antibody *my32* [16, 30] and seem to be of the superfast phenotype. To evaluate the effect of only considering superfast fibers we corrected all muscle fiber counts and found the effect to be <1 %.

Spatiotemporal resolved Calcium imaging in an intact muscle cross-section.—To image the time resolved calcium kinetics of a whole muscle, while sparsely stimulating motor neuron axons, we developed a nerve-muscle preparation consisting of the *musculus syringealis dorsalis medialis* (MDS) and the entire tracheosyringeal section of the hypoglossal nerve (NXIIts). We focused on the female MDS, as this is the thinnest intrinsic syringeal muscle that allowed full penetration with confocal microscopy. To prevent damaging nerves and muscle fibers during dissection, the preparation also included all dorsal muscles from left to right DTB (see Figure 3B), including the tissues they attach to. Animals were euthanized with an overdose of isoflurane and the syrinx including the entire trachea was rapidly dissected out and submerged in ice-cold dissection buffer (150 mM NaCl, 2.5 mM KCl, 0.5 mM $CaCl_2$, 1 mM NaH_2PO_4, 6.5 mM $MgSO_4$, 10 mM Hepes, 12 mM Glucose, pH 7.4 adjusted with a 1 M Trizma solution). After carefully preparing the dorsal muscle group off the syrinx, both NXIIts nerves were dissected off the trachea over approximately 30 mm. The preparation was then mounted into a custom-build liquid-cooled imaging chamber. The MDS was placed as close to the glass bottom of the chamber as possible. The nerve was led into a separate subsection of the chamber and secured on a Sylgard pad. The entire preparation was then incubated in a 2 mg/ml Collagenase (Collagenase Type 4 (C. histolyticum) P5275, Abnova) solution for 20 minutes at 30 °C. After washing the preparation with fresh, cold dissection buffer, the epineurium was removed and the nerve was carefully separated into a fan using sharp tungsten wires to enable sparse stimulation. Subsequently, the preparation was washed with recording buffer (150 mM NaCl, 2.5 mM KCl, 4 mM $CaCl_2$, 1 mM NaH_2PO_4, 1 mM $MgSO_4$, 10 mM Hepes,

12 mM Glucose, pH 7.4 adjusted with a 1 M Trizma solution) and incubated with recording buffer supplemented with 20 μM myosin inhibitor (N-benzyl-p-toluene sulphonamide (BTS), 203895, Sigma) [66] and 25 μM Calcium indicator (Cal-520 AM, ab171868, abcam) solution for 15 minutes at 30 °C and additional 45 minutes at room temperature. Before starting the data acquisition, the preparation was washed again with recording buffer containing 20 μM BTS. For imaging the muscle preparation was submerged in imaging solution (recording buffer with 20 μM BTS containing 34 % (v/v) Optiprep medium, D1556, Sigma) to match the refractive index of the medium as closely as possible to the muscle tissue [67]. On the nerve side of the chamber, we overlayed the water based medium with paraffine oil, so that the stimulation site/nerve fan was completely submerged in oil [68], while the rest of the nerve rested in imaging solution. The chamber was then mounted on the microscope stage and liquid-cooled to 10°C (Julabo F12-ED).

Imaging was performed on a Leica SP8 inverted microscope equipped with a fast resonant scanner (8kHz) and a Leica HC PL 40x/1,1 IRAPO objective with correction ring. The calcium indicator was excited with an argon laser at 488 nm. The Cal-520 signal was detected with a hybrid (HyD) detector in photon counting mode and gating (0.3 ns - 6 ns) set to 512 – 575 nm. Imaging width was fixed at 235.5 μm and depth in z-direction was adjusted to accommodate the entire preparation. Scan settings were optimized for the fastest possible image acquisition (31 Hz, bidirectional scanning, resolution of 1.168 μm). Images were acquired at 12-bit resolution. Motion correction was performed using the TurboReg plugin (Rigid body, accurate mode) [69] for ImageJ (v1.53e) [70].

Sections of the NXIIts fan were locally stimulated using a four-electrode array consisting of 50 μm silver wire electrodes connected to linear stimulus isolators (WPI, A395). Per electrode, we applied 10 mono-phasic stimulations at 4 Hz at fixed current. To increase the injected energy, we increased the duration of these stimulations stepwise from 10 to 1000 μs in 50 μs steps (*Nerve Stimulation series*). Injected energy was approximated as the injected current times stimulation duration. After completing this series on the four electrodes, we ensured which muscle fibers were alive by field-stimulation of the entire muscle between two platinum electrodes connected to a high-power muscle stimulator (Aurora Scientific, model 701C). We applied 40 – 100 pulses (1 ms, 24 V) at 4 Hz (*Muscle stimulation series*). To obtain the structure of the muscle fibers within the muscle, we lastly imaged a series of 3000 images without any stimulation (*Structural series*). If the muscle did not fit entirely in the frame, we moved the stage and repeated the above procedure with 15 – 30 % overlap between regions. All stimulation control software was written in Matlab (MathWorks, RRID: SCR_001622). To synchronize the stimulation trigger data with the microscope we send a 100 ms 10 V pulse to a green LED mounted above the objective. All stimulation/sync output and input triggers were written and digitized at 200 kHz (NI DAQ USB-6259, National Instruments).

To identify all muscle fibers in the preparation we computed the mean image of the autofluorescence in the structural series (Figure 3C) and used this image to manually locate the centers of all muscle fibers. We created an image mask containing the muscle fibers by placing a circle with a radius of three pixels in the fiber centers (using Matlab functions *strel* and *imdilate*). Next, we identified the living muscle fibers by detecting the frames with

Cal520 fluorescence peaks in the motion-corrected *Muscle stim series.* We calculated the relative difference of the fluorescence signal (dF/F or dFF) per muscle fiber per stimulation by comparing the intensity (F) in the frames with stimulation and three frames prior to stimulation (dF). To test if a MF was alive, we tested if the dFF signal for the 40 – 100 stimuli was different from 0 with a paired Student t-test with p divided by the number of detected stimuli (significance was accepted for $p < 0.01$). This low p values ($1.0e^{-4}$ - $2.5e^{-4}$) gave very conservative estimates of alive fibers that reflected our observations.

To identify individual MUs in the motor nerve stimulations, we synchronized the stimulation trigger data with the imaging data and computed the dFF signal of all muscle fibers in the motion-corrected, masked *nerve stimulation series.* The stepwise increasing stimulus energy resulted in the activation of an increasing number of MUs. We first used an automated procedure to identify all active muscle fibers. We upsampled the dFF signals for all fibers to 1 kHz using a polyphase antialiasing filter (*resample* function). We isolated the 20 – 100 ms dFF segment after each stimulus and calculated the mean dFF signal for the 10 repeated stimuli per stimulus energy step. A spike was detected if the averaged dFF signal passed a certain threshold that was fixed for all MFs within a preparation. This resulted in a spike raster for all MFs. MFs that belonged to the same MU would start firing at the same stimulus energy level and thus sorting the spike raster for onset timing would identify Mus and result in a distribution of MU sizes per electrode. Subsequently, IA and CPHE manually checked the correlation between pattern onset and activity in the raw dFF signals between muscle fibers for all identified MUs. This procedure was repeated for all electrodes.

Muscle specific tension.—We characterized muscle specific tension of the *musculus syringealis ventralis* (VS; n = 5), *musculus tracheobonchealis ventralis* (VTB; n =5), and *musculus tracheobonchealis dorsalis* (DTB; n = 7) of adult male zebra fiches on preparations of isolated muscle fiber bundles as previously described [71]. In brief, fiber bundles were mounted in a temperature-controlled bath, which was continuously supplied with oxygenated Ringers solution. The rostral end of the preparation was fixed to a force transducer (Model 400A, Aurora Scientific) and the caudal end to a micromanipulator, which was used to control length of the preparation. Field stimulations were applied through platinum wire electrodes using a high-power muscle stimulator (Aurora Scientific, model 701C). Force and stimulation signals were low pass filtered (EF120 BNC through-feed low-pass filter, Thor Labs) and digitized at 40 kHz (NI DAQ Board PCI-MIO-16E4, National Instruments). The force baseline was defined as the average amplitude of 50 ms of the force signal prior to stimulation onset and subtracted from all force data.

To measure P_o, we optimized first stimulation amplitude (at pulse width of 300 μs) for maximal force production, followed by tetanic force frequency curve by 100 ms pulse trains ranging from 100 – 800 Hz in 100 Hz steps, and finally resting length L_o. Isometric stress was calculated as F/A_{csa} of the muscle, where the cross-sectional area A_{csa} was estimated from the resting length L_o and the dry weight (dry-wet conversion factor: 5) of the muscle fibers assuming a constant density of 1060 kg/m^3 from [72]. Muscle specific force was calculated using the average CSA as in Table S1. Similarly, the force per muscle fiber was obtained by dividing the muscle specific force by the average number of muscle fibers as in Table S1. We determined the P_o of bat superfast laryngeal muscle by re-analyzing previously

published data [73]. All control software was written in Matlab (MathWorks, RRID: SCR_001622) and all analyses were performed in R v. 3.6.1 [74].

In vitro sound production.—We developed an experimental paradigm that allowed for sound production *in vitro* building on earlier work. Previously, we induced syringeal sound production by precisely controlling bronchial and air sac pressure *in vitro* or in perfused preparations *ex vivo* [42]. Additionally, we developed methods to actuate muscle insertion sites but without inducing sound [7]. Here we further developed our experimental chamber and combined sound induction by pressure control with the actuation of a single syringeal muscle insertion site and force measurements. In brief, directly after syrinx extraction, the *musculus syringealis ventralis* (VS) was removed while the syrinx was still submerged in Ringers solution. The syrinx was then moved to the experimental chamber and a 10–0 suture needle was inserted through the center of the bottom edge of the *medio-ventral cartilage* (MVC) pads. The uni-filament suture was threaded through a 100 μm hole and attached to a servomotor (Ergometer model 322C, Aurora Scientific) that controlled length while measuring force at the tip of the lever arm (displacement and force resolution 1 μm and 0.3 mN, respectively). To induce sound, we applied a pressure differential over the syringeal labia (air sac pressure 2.0 kPa, bronchial pressure 1.0 kPa) using dual-valve differential pressure PID Controllers (model PCD, 0 – 10 kPa, Alicat Scientific). Next, we actuated the MVC in a 500 ms ramp from 0 to maximally 12 % of the VS length [7], and measured the corresponding shift in f_0 in 5 syrinx preparations.

Sound was recorded with a ½-inch pressure microphone-pre-amplifier assembly (model 46AD with preamplifier type 26AH, G.R.A.S., Denmark), amplified and high-pass filtered (10 Hz, 3-pole Butterworth filter, model 12AQ, G.R.A.S.). The microphone sensitivity was measured before each experiment (sound calibrator model 42AB, G.R.A.S.). The microphone was placed at 2 – 3 cm from the tracheal connector outlet in the acoustic near field, and on a 45° angle to avoid the air jet from the tracheal outlet.

Microphone, pressure, force, and displacement signals were low-pass filtered at 10 kHz (EF120 BNC through-feed low-pass filter, Thor Labs) and digitized at 50 kHz (NI DAQ USB-6259, National Instruments). We calculated the mean values for pressure, force and displacement signals in 2 ms bins with a 1 ms sliding window. To calculate f_0 for each bin, we used the Yin algorithm [75] within a frequency range of 350 – 1300 Hz, and aperiodicity threshold between 0.1 – 0.2. All control and analysis software was written in Matlab (MathWorks, RRID: SCR_001622).

Quantification and Statistical Analysis

Statistics.—All analyses were performed in Matlab or R v. 3.6.1. The Welch Two Sample t-test was used to test for significant differences between left and right NXIIts axon and muscle fiber numbers. Root innervation numbers were pooled across left and right syrinx halves when not significantly different ($p > 0.05$). Statistical difference between force production by VS, VTB and DTB muscles was assessed using ANOVA.

The VS force (x) -f_0 (y) transformation was modeled with a linear model at low force and an exponential model at high force [76]:

$$y = \begin{cases} a + bx, x \leq x_0 \\ Ae^{Bx}, x > x_0 \end{cases}, \quad \text{Eq 2}$$

where x_0 is the linear limit. To satisfy the continuous and differentiable requirements, we set $a + bx_0 = Ae^{Bx\epsilon 0}$ and $b = ABe^{Bx0}$, and thus the linear limit is $x_0 = \frac{1}{B} - \frac{a}{b}$. The parameters were determined by iteratively optimizing the model fit minimizing least squares using the MATLAB routine *lsqcurvefit.*

Supplementary Material

Refer to Web version on PubMed Central for supplementary material.

Acknowledgments.

The authors wish to thank Torben Christensen, Per Martensen, Morten Ebbesen, Sonja Jacobsen and Bianca Jørgensen for technical support, and Samuel Sober for comments on the manuscript. This study was funded support from the Carlsberg foundation (CF17-0949) and the Danish Research Council (DFF 5051-00195) to IA and by support from the Novo Nordisk Foundation (NNF17OC0028928) and National Institutes of Health (1R01NS099375) to CPHE.

References

1. Price T (1998). Sexual selection and natural selection in bird speciation. Philos T R Soc B 353, 251–260.
2. Uy JAC, Irwin DE, and Webster MS (2018). Behavioral Isolation and Incipient Speciation in Birds. Annu Rev Ecol Evol S 49, 1–24.
3. Janik VM, and Slater PJ (2000). The different roles of social learning in vocal communication. Anim Behav 60, 1–11. [PubMed: 10924198]
4. Gaunt AS (1983). An Hypothesis Concerning the Relationship of Syringeal Structure to Vocal Abilities. Auk 100, 853–862.
5. Titze I, Riede T, and Mau T (2016). Predicting Achievable Fundamental Frequency Ranges in Vocalization Across Species. PLoS Comput Biol 12, e1004907. [PubMed: 27309543]
6. Goller F, and Riede T (2013). Integrative physiology of fundamental frequency control in birds. J Physiol Paris 107, 230–242. [PubMed: 23238240]
7. During DN, Knorlein BJ, and Elemans CPH (2017). In situ vocal fold properties and pitch prediction by dynamic actuation of the songbird syrinx. Sci Rep 7, 11296. [PubMed: 28900151]
8. Fee MS, and Scharff C (2010). The songbird as a model for the generation and learning of complex sequential behaviors. Ilar J 51, 362–377. [PubMed: 21131713]
9. Vicario DS, and Nottebohm F (1988). Organization of the zebra finch song control system: I. Representation of syringeal muscles in the hypoglossal nucleus. J Comp Neurol 271, 346–354. [PubMed: 3385013]
10. Adam I, and Elemans CPH (2019). Vocal Motor Performance in Birdsong Requires Brain-Body Interaction. eNeuro 6.
11. Xiao L, Chattree G, Oscos FG, Cao M, Wanat MJ, and Roberts TF (2018). A Basal Ganglia Circuit Sufficient to Guide Birdsong Learning. Neuron 98, 208–221 e205. [PubMed: 29551492]
12. Sober SJ, and Brainard MS (2009). Adult birdsong is actively maintained by error correction. Nat Neurosci 12, 927–931. [PubMed: 19525945]
13. Tumer EC, and Brainard MS (2007). Performance variability enables adaptive plasticity of 'crystallized' adult birdsong. Nature 450, 1240–1244. [PubMed: 18097411]
14. Enoka RM, and Fuglevand AJ (2001). Motor unit physiology: some unresolved issues. Muscle Nerve 24, 4–17. [PubMed: 11150961]

15. Tang C, Chehayeb D, Srivastava K, Nemenman I, and Sober SJ (2014). Millisecond-scale motor encoding in a cortical vocal area. PLoS Biol 12, e1002018. [PubMed: 25490022]
16. Christensen LA, Allred LM, Goller F, and Meyers RA (2017). Is sexual dimorphism in singing behavior related to syringeal muscle composition? The Auk 134, 710–720.
17. Lissandrello CA, Gillis WF, Shen J, Pearre BW, Vitale F, Pasquali M, Holinski BJ, Chew DJ, White AE, and Gardner TJ (2017). A micro-scale printable nanoclip for electrical stimulation and recording in small nerves. J Neural Eng 14, 036006. [PubMed: 28323640]
18. Lohmann R, and Gahr M (2000). Muscle-dependent and hormone-dependent differentiation of the vocal control premotor nucleus robustus archistriatalis and the motornucleus hypoglossus pars tracheosyringealis of the zebra finch. J Neurobiol 42, 220–231. [PubMed: 10640329]
19. Santo Neto H, and Marques MJ (2008). Estimation of the number and size of motor units in intrinsic laryngeal muscles using morphometric methods. Clin Anat 21, 301–306. [PubMed: 18428996]
20. Hinrichsen CF, and Ryan A (1982). The size of motor units in laryngeal muscles of the rat. Experientia 38, 360–361. [PubMed: 6176466]
21. Mühlendyck H (1978). The Size of Motor Units in Reference to Eye-Muscle Fibres of Different Innervation. (Munich: J.F. Bergmann-Verlag), pp. 17–26.
22. During DN, Ziegler A, Thompson CK, Ziegler A, Faber C, Muller J, Scharff C, and Elemans CP (2013). The songbird syrinx morphome: a three-dimensional, high-resolution, interactive morphological map of the zebra finch vocal organ. BMC Biol 11, 1. [PubMed: 23294804]
23. Raikova R, Celichowski J, Angelova S, and Krutki P (2018). A model of the rat medial gastrocnemius muscle based on inputs to motoneurons and on an algorithm for prediction of the motor unit force. J Neurophysiol 120, 1973–1987. [PubMed: 30020845]
24. Elek JM, Kossev A, Dengler R, Schubert M, Wohlfahrt K, and Wolf W (1992). Parameters of Human Motor Unit Twitches Obtained by Intramuscular Microstimulation. Neuromuscular Disord 2, 261–267.
25. Milner-Brown HS, Stein RB, and Yemm R (1973). The orderly recruitment of human motor units during voluntary isometric contractions. J Physiol 230, 359–370. [PubMed: 4350770]
26. Olson CB, and Swett CP (1966). A Functional and Histochemical Characterization of Motor Units in a Heterogeneous Muscle (Flexor Digitorum Longus) of Cat. Journal of Comparative Neurology 128, 475–&.
27. McPhedran AM, Wuerker RB, and Henneman E (1965). Properties of Motor Units in a Homogeneous Red Muscle (Soleus) of the Cat. J Neurophysiol 28, 71–84. [PubMed: 14244797]
28. Lu J, Tapia JC, White OL, and Lichtman JW (2009). The interscutularis muscle connectome. PLoS Biol 7, e32. [PubMed: 19209956]
29. Hirst TC, and Ribchester RR (2013). Segmentation of the mouse fourth deep lumbrical muscle connectome reveals concentric organisation of motor units. J Physiol 591, 4859–4875. [PubMed: 23940381]
30. Mead AF, Osinalde N, Ortenblad N, Nielsen J, Brewer J, Vellema M, Adam I, Scharff C, Song Y, Frandsen U, et al. (2017). Fundamental constraints in synchronous muscle limit superfast motor control in vertebrates. Elife 6.
31. Haugen I-B, and Bruenech J (2005). Histological analysis of the efferent innervation of human extraocular muscle fibres.
32. Schiaffino S, and Reggiani C (2011). Fiber types in mammalian skeletal muscles. Physiol Rev 91, 1447–1531. [PubMed: 22013216]
33. Decroix L, Van Muylder V, Desender L, Sampaolesi M, and Thorrez L (2015). Tissue clearing for confocal imaging of native and bio-artificial skeletal muscle. Biotech Histochem 90, 424–431. [PubMed: 25893542]
34. Llewellyn ME, Thompson KR, Deisseroth K, and Delp SL (2010). Orderly recruitment of motor units under optical control in vivo. Nat Med 16, 1161–U1144. [PubMed: 20871612]
35. Sober SJ, Sponberg S, Nemenman I, and Ting LH (2018). Millisecond Spike Timing Codes for Motor Control. Trends Neurosci 41, 644–648. [PubMed: 30274598]
36. Elemans CP, Mead AF, Rome LC, and Goller F (2008). Superfast vocal muscles control song production in songbirds. PLoS One 3, e2581. [PubMed: 18612467]

37. Rome LC, and Lindstedt SL (1998). The Quest for Speed: Muscles Built for High-Frequency Contractions. News Physiol Sci 13, 261–268. [PubMed: 11390801]
38. Elemans CP, Spierts IL, Hendriks M, Schipper H, Muller UK, and van Leeuwen JL (2006). Syringeal muscles fit the trill in ring doves (Streptopelia risoria L.). J Exp Biol 209, 965–977. [PubMed: 16481585]
39. Brooks SV, and Faulkner JA (1991). Forces and powers of slow and fast skeletal muscles in mice during repeated contractions. J Physiol 436, 701–710. [PubMed: 2061852]
40. Urbanchek MG, Picken EB, Kalliainen LK, and Kuzon WM Jr. (2001). Specific force deficit in skeletal muscles of old rats is partially explained by the existence of denervated muscle fibers. J Gerontol A Biol Sci Med Sci 56, B191–197. [PubMed: 11320099]
41. Srivastava KH, Elemans CP, and Sober SJ (2015). Multifunctional and Context-Dependent Control of Vocal Acoustics by Individual Muscles. J Neurosci 35, 14183–14194. [PubMed: 26490859]
42. Elemans CP, Rasmussen JH, Herbst CT, During DN, Zollinger SA, Brumm H, Srivastava K, Svane N, Ding M, Larsen ON, et al. (2015). Universal mechanisms of sound production and control in birds and mammals. Nat Commun 6, 8978. [PubMed: 26612008]
43. Goller F, and Suthers RA (1996). Role of syringeal muscles in controlling the phonology of bird song. J Neurophysiol 76, 287–300. [PubMed: 8836225]
44. Goller F, and Suthers RA (1996). Role of syringeal muscles in gating airflow and sound production in singing brown thrashers. J Neurophysiol 75, 867–876. [PubMed: 8714659]
45. Rome LC, Cook C, Syme DA, Connaughton MA, Ashley-Ross M, Klimov A, Tikunov B, and Goldman YE (1999). Trading force for speed: why superfast crossbridge kinetics leads to superlow forces. Proc Natl Acad Sci U S A 96, 5826–5831. [PubMed: 10318969]
46. Young IS, and Rome LC (2001). Mutually exclusive muscle designs: the power output of the locomotory and sonic muscles of the oyster toadfish (Opsanus tau). Proceedings. Biological sciences / The Royal Society 268, 1965–1970.
47. Ellerby DJ, and Askew GN (2007). Modulation of flight muscle power output in budgerigars Melopsittacus undulatus and zebra finches Taeniopygia guttata: in vitro muscle performance. J Exp Biol 210, 3780–3788. [PubMed: 17951419]
48. Düring DN, and Elemans CPH (2016). Embodied Motor Control of Avian Vocal Production. In Vertebrate Sound Production and Acoustic Communication, Suthers RA, Fitch WT, Fay RR and Popper AN, eds. (Cham: Springer International Publishing), pp. 119–157.
49. Riede T, and Goller F (2010). Functional morphology of the sound-generating labia in the syrinx of two songbird species. J Anat 216, 23–36. [PubMed: 19900184]
50. Fee MS (2002). Measurement of the linear and nonlinear mechanical properties of the oscine syrinx: implications for function. J Comp Physiol A Neuroethol Sens Neural Behav Physiol 188, 829–839. [PubMed: 12471484]
51. Pfeifer R, Lungarella M, and Iida F (2007). Self-organization, embodiment, and biologically inspired robotics. Science 318, 1088–1093. [PubMed: 18006736]
52. Ramaswamy KS, Palmer ML, van der Meulen JH, Renoux A, Kostrominova TY, Michele DE, and Faulkner JA (2011). Lateral transmission of force is impaired in skeletal muscles of dystrophic mice and very old rats. J Physiol 589, 1195–1208. [PubMed: 21224224]
53. Huijing PA (1999). Muscle as a collagen fiber reinforced composite: a review of force transmission in muscle and whole limb. J Biomech 32, 329–345. [PubMed: 10213024]
54. Andalman AS, and Fee MS (2009). A basal ganglia-forebrain circuit in the songbird biases motor output to avoid vocal errors. Proc Natl Acad Sci U S A 106, 12518–12523. [PubMed: 19597157]
55. Prior NH, Smith E, Lawson S, Ball GF, and Dooling RJ (2018). Acoustic fine structure may encode biologically relevant information for zebra finches. Sci Rep-Uk 8.
56. Lohr B, and Dooling RJ (1998). Detection of changes in timbre and harmonicity in complex sounds by zebra finches (Taeniopygia guttata) and budgerigars (Melopsittacus undulatus). J Comp Psychol 112, 36–47. [PubMed: 9528113]
57. Woolley SC, and Doupe AJ (2008). Social context-induced song variation affects female behavior and gene expression. PLoS Biol 6, e62. [PubMed: 18351801]
58. Bruenech JR, and Kjellevold Haugen IB (2015). How does the structure of extraocular muscles and their nerves affect their function? Eye (Lond) 29, 177–183. [PubMed: 25397785]

59. Feduccia A (2003). 'Big bang' for tertiary birds? Trends in Ecology & Evolution 18, 172–176.
60. King A (1989). Functional anatomy of the syrinx. In Form and Function in Birds, Volume 4, King A and McLelland J, eds. (London, UK: Academic Press), pp. 105–192.
61. Moore JM, Szekely T, Buki J, and Devoogd TJ (2011). Motor pathway convergence predicts syllable repertoire size in oscine birds. Proc Natl Acad Sci U S A 108, 16440–16445. [PubMed: 21918109]
62. Faunes M, Botelho JF, and Wild JM (2017). Innervation of the syrinx of the zebra finch (Taeniopygia guttata). J Comp Neurol 525, 2847–2860. [PubMed: 28472866]
63. Bottjer SW, and Arnold AP (1982). Afferent neurons in the hypoglossal nerve of the zebra finch (Poephila guttata): localization with horseradish peroxidase. J Comp Neurol 210, 190–197. [PubMed: 7130479]
64. Bottjer SW, and To M (2012). Afferents from vocal motor and respiratory effectors are recruited during vocal production in juvenile songbirds. J Neurosci 32, 10895–10906. [PubMed: 22875924]
65. Fuglevand AJ, Winter DA, and Patla AE (1993). Models of recruitment and rate coding organization in motor-unit pools. J Neurophysiol 70, 2470–2488. [PubMed: 8120594]
66. Cheung A, Dantzig JA, Hollingworth S, Baylor SM, Goldman YE, Mitchison TJ, and Straight AF (2002). A small-molecule inhibitor of skeletal muscle myosin II. Nat Cell Biol 4, 83–88. [PubMed: 11744924]
67. Boothe T, Hilbert L, Heide M, Berninger L, Huttner WB, Zaburdaev V, Vastenhouw NL, Myers EW, Drechsel DN, and Rink JC (2017). A tunable refractive index matching medium for live imaging cells, tissues and model organisms. Elife 6.
68. Drzymala-Celichowska H, and Celichowski J (2020). Functional Isolation of Single Motor Units of Rat Medial Gastrocnemius Muscle. J Vis Exp
69. Thevenaz P, Ruttimann UE, and Unser M (1998). A pyramid approach to subpixel registration based on intensity. IEEE Trans Image Process 7, 27–41. [PubMed: 18267377]
70. Schindelin J, Rueden CT, Hiner MC, and Eliceiri KW (2015). The ImageJ ecosystem: An open platform for biomedical image analysis. Mol Reprod Dev 82, 518–529. [PubMed: 26153368]
71. Srivastava KH, Holmes CM, Vellema M, Pack AR, Elemans CPH, Nemenman I, and Sober SJ (2017). Motor control by precisely timed spike patterns. P Natl Acad Sci USA 114, 1171–1176.
72. Mendez J, and Keys A (1960). Density and Composition of Mammalian Muscle. Metabolism 9, 184–188.
73. Elemans CP, Mead AF, Jakobsen L, and Ratcliffe JM (2011). Superfast muscles set maximum call rate in echolocating bats. Science 333, 1885–1888. [PubMed: 21960635]
74. R Core Team (2019). R: A Language and Environment for Statistical Computing. R Foundation for Statistical Computing, Vienna, Austria.
75. de Cheveigne A, and Kawahara H (2002). YIN, a fundamental frequency estimator for speech and music. J Acoust Soc Am 111, 1917–1930. [PubMed: 12002874]
76. Zhang YS, Takahashi DY, Liao DA, Ghazanfar AA, and Elemans CPH (2019). Vocal state change through laryngeal development. Nat Commun 10, 4592. [PubMed: 31597928]

Highlights

- Motor neurons in the zebra finch vocal motor pool innervate single muscle fibers
- Zebra finch vocal muscles have the lowest measured isometric stress
- Small motor unit size and low muscle stress provide sub-Hz pitch control resolution
- High-resolution control was key to vocal space expansion and songbird radiation

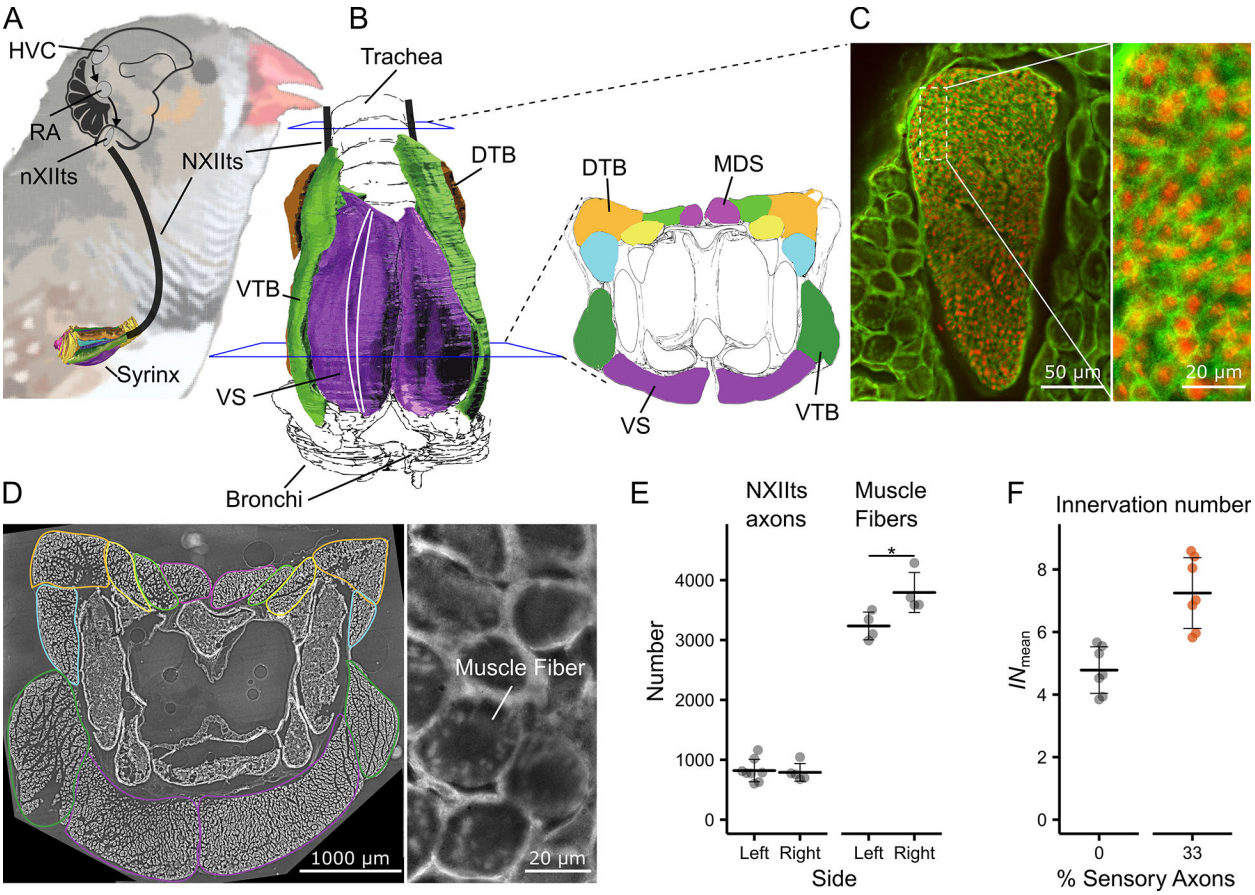

Figure 1. The songbird syrinx motor pool has very low mean innervation numbers.

A) Schematic of the motor control pathway of the songbird syrinx. B) Ventral view (left) and cross-section (right) of the syrinx with muscles highlighted in color. All muscle fibers run in parallel from rostral to caudal [22] as indicated by two white lines on the ventral view. C) Cross-sections through the tracheosyringeal branch of the hypoglossal nerve (NXIIts) and D) the syrinx (~800 stitched images) at mid-level, where all muscle fibers are present. The individual muscles are outlined in the same colors as in the cross-section in B. E) NXIIts axon and muscle fiber number and F) IN_{mean} per individual for a minimum estimate of 0 % (grey) and a maximum of 33 % (orange) sensory axons within NXIIts. See also Table S1. Data presented as mean ± SD. HVC: used as proper name, RA: robust nucleus of the arcopallium, nXIIts: tracheosyringeal portion of the hypoglossal nucleus, NXIIts: tracheosyringeal part of the hypoglossal nerve, DTB: *musculus tracheobonchealis dorsalis,* MDS: *musculus syringealis dorsalis medialis,* VS: *musculus syringealis ventralis,* VTB: *musculus tracheobonchealis ventralis,* * at $p < 0.05$.

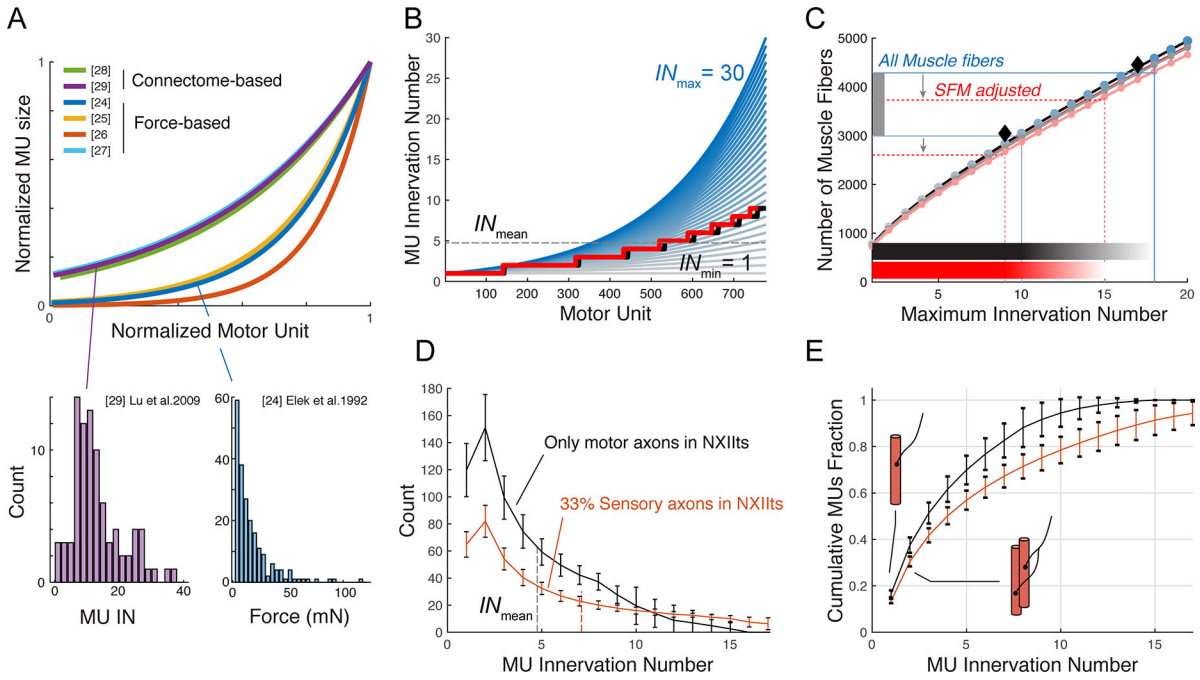

Figure 2. MU size distribution models predict one-to-one innervation in the songbird syrinx motor pool.

A) MU size distributions are skewed towards small units (bottom) and exponential in both anatomical connectome reconstructions and force-based measurements (top, and Figure S1). B) *IN* distribution as function of MU with IN_{max} ranging from 1 (gray) to 30 (blue). Black lines indicate the average IN_{mean} (horizontal dotted line) and distributed *IN* (stepped line) for the individual with the smallest IN_{mean} (3.84). The red line (also next panel) indicates the distribution for only superfast muscle fibers. See also Figure S2. C) The number of muscle fibers (horizontal lines) provides IN_{max} per individual. Colors correspond to IN_{max} lines in panel B. Shown are the individuals with smallest (3.84, gray) and largest IN_{mean} (5.67, blue). Shaded horizontal bars indicate *IN* range. D) Distribution and E) cumulative fraction of MU as a function of *IN* for superfast fibers with 0% (black line) or 33 *%* (orange line) adjustment for afferent sensory axons. Data presented as mean ± SD.

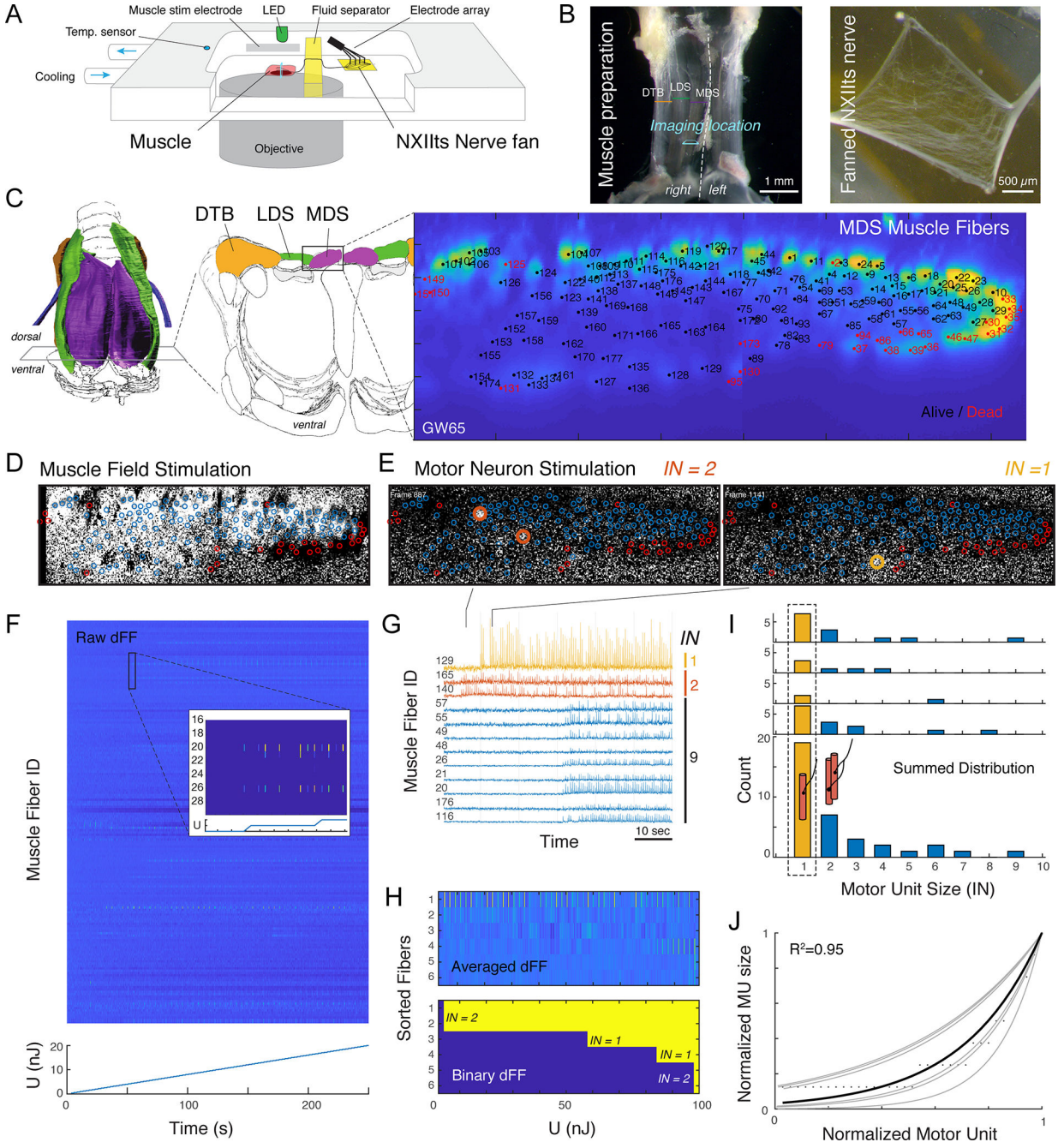

Figure 3. The songbird syrinx motor pool has functional one-to-one innervation.

A) Schematic of setup to measure spatiotemporal resolved calcium spikes across the cross-section of an entire muscle. B) The muscle-nerve preparation (left) and fanned NXIIts nerve (right). C) Cross-section through the alive MDS muscle (3000 averages) showing all identified muscle fibers. D) Calcium dFF signal during field stimulation of the entire muscle shows alive (blue circles) and dead (red circles) muscle fibers. E) Example dFF frames during single motor nervlet stimulation of a motor unit with *IN* = 2 (left, muscle fibers 140 & 165) and *IN* = 1 (right, muscle fiber 129). F) Intensity color-coded raw dFF traces of all 172 muscle fibers during stepwise increase of the injected energy during 4 Hz stimulation by

a single electrode. G) Raw dFF traces of 12 muscle fibers showing three MUs with *IN* = 1, 2 and 9, respectively. H) 10x averaged (top) and binary (bottom) dFF signal of active muscle fibers, sorted for onset timing showing two MUs with *IN* = 1 and two with *IN* = 2. I) Individual (top) and summed (bottom) *IN* distribution show that all individuals had several MUs that innervated a single muscle fiber (yellow bars). J) The summed distribution follows an exponential distribution (black line) that falls within the known MU distributions in other muscles [24–29] (gray lines, Figure 2A, S1). See also Video S1.

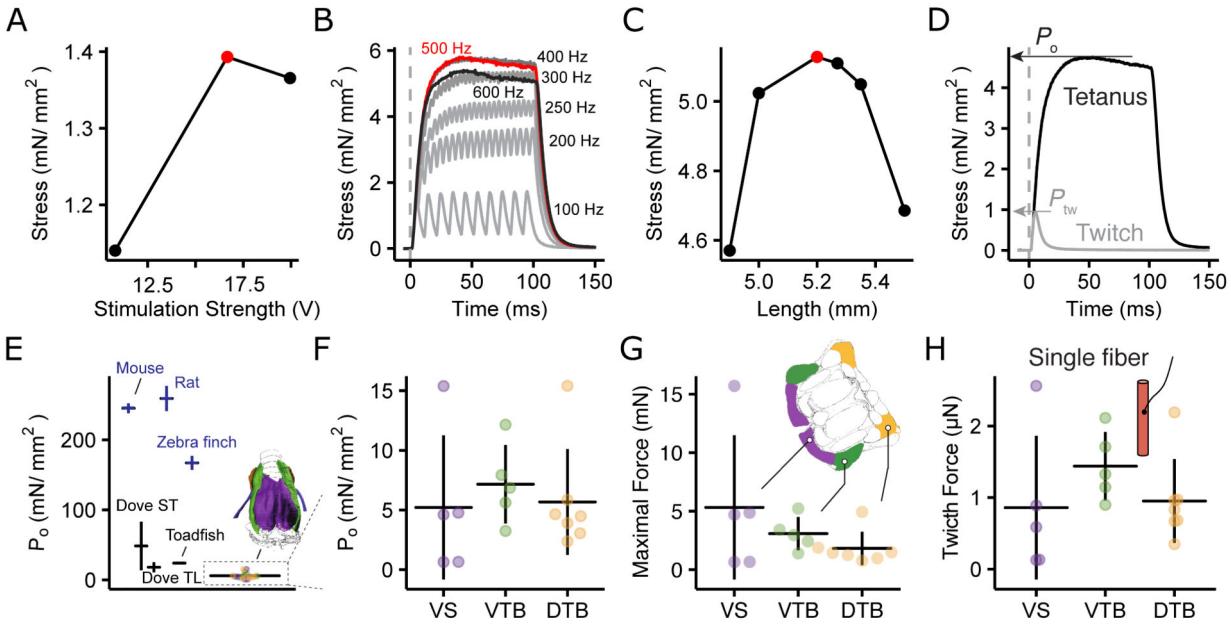

Figure 4. Songbird syringeal muscles generate the lowest stress.

Optimization of A) stimulus amplitude, B) frequency and C) muscle fiber length to determine P_o. D) Force profile after single (twitch) and tetanic (500 Hz) stimulation. Traces are the mean of eight twitch and three 500 Hz stimulations. E) P_o for syringeal muscles is 30 – 60x lower than skeletal (dark blue) muscles. F) P_o does not differ significantly between muscles (ANOVA: F = 0.24, df = 2 and 14, p = 0.79) G) Maximal force per muscle. H) Single fiber twitch force is not significantly different between muscles (ANOVA: F = 0.997, df = 2 and 14, p = 0.39)

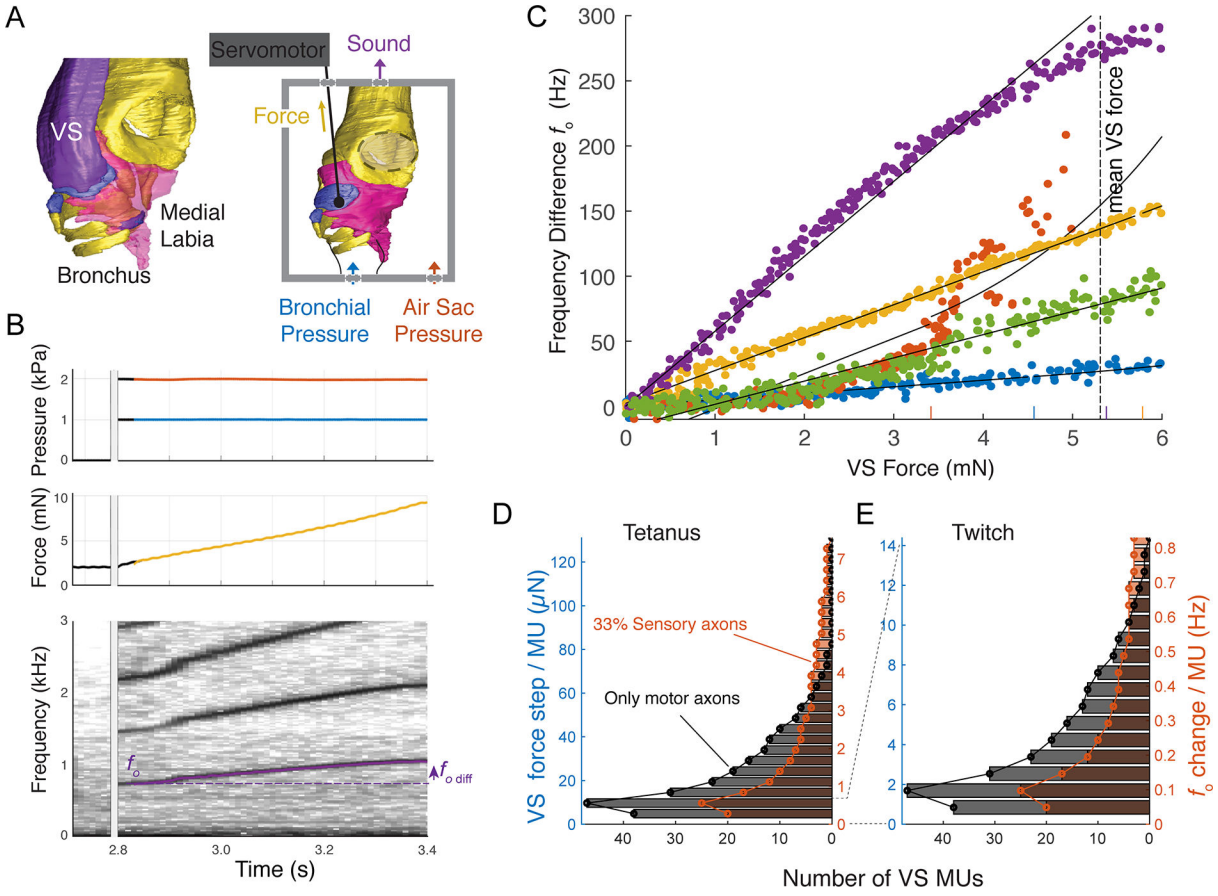

Figure 5. Syringeal MUs provide sub-Hertz resolution control of fundamental frequency.

A) Sound production paradigm *in vitro* actuating the insertion site of the f_0 controlling ventral syringeal (VS) muscle. B) Example raw data of sound production induced by raising pressure (top), slow VS force modulation (middle) and resulting f_0 changes (bottom). C) Frequency change as a function of VS force is linear over half the range of the average VS force modulation range of 0 – 5.31 mN in all 5 individuals (color coded). Short vertical lines on the x-axis indicate break point between linear and exponential curve fit for all individuals. See also Table S2. D) Distribution of the number of MUs within VS per force and f_0 step available during maximal (tetanic) and E) minimal (twitch) force development.

KEY RESOURCES TABLE

REAGENT or RESOURCE	SOURCE	IDENTIFIER
Antibodies		
rabbit-anti-Laminin	Sigma-Aldrich	Cat# L9393, RRID: AB_477163
mouse-anti-Neurofilament	Millipore	Cat# CBL212, RRID: AB_93408
donkey-anti-mouse-Alexa-Fluor-568	Abcam	Cat# ab175700
donkey-anti-rabbit-Alexa-Fluor-488	Abcam	Cat# ab150061, RRID: AB_2571722
Biological samples		
Male zebra finch syrinxes	Elemans laboratory SDU, Denmark	NA
Female zebra finch syrinxes	Elemans laboratory SDU, Denmark	NA
Chemicals, peptides, and recombinant proteins		
Vectashield	Vector Laboratories	Cat# H-1000, RRID: AB_2336789
N-benzyl-p-toluene sulphonamide (BTS)	Sigma	Cat# 203895
Cal-520 AM	Abcam	Cat# ab171868
Collagenase Type 4 (C. histolyticum)	Abnova	Cat# P5275
Optiprep medium	Sigma	Cat# D1556
Experimental models: Organisms/strains		
Zebra finch *Taeniopygia guttata*	Own breeding, Elemans laboratory SDU, Denmark	NA
Software and algorithms		
Matlab	MathWorks	RRID: SCR_001622; Version 2020a
TurboReg for ImageJ	[69]	http://bigwww.epfl.ch/thevenaz/turboreg/
ImageJ	[70]	https://imagej.net/Welcome
R	The R foundation[74]	https://www.r-project.org/
Yin algorithm	[75]	http://audition-backend.ens.fr/adc/
Other		
8kHz Resonant scanner	Leica	NA
High-power muscle stimulator	Aurora Scientific	Cat# 701C
Linear Stimulus Isolator	WPI	Cat# A395
NI DAQ	National Instruments	USB-6259
In vitro servo controlled syrinx setup	This study	NA
Force transducer	Aurora Scientific	Cat# 400A
In vitro muscle physiology setup	Srivastana et al.[71]	NA
Ergometer	Aurora Scientific	Cat# 322C
½-inch pressure microphone	G.R.A.S. Denmark	Cat# 46AD
Pre-amplifier	G.R.A.S. Denmark	Cat# 26AH
Sound calibrator	G.R.A.S. Denmark	Car# 12AQ